ACS OMEGA

http://pubs.acs.org/journal/acsodf

Article

Identification and Elemental Impurity Analysis of Heterogeneous Morphologies in Uranium Oxides Synthesized from Uranyl Fluoride Precursors

Cody A. Nizinski, Jacob Olson, Aaron M. Chalifoux, Nick Kurtyka, Matthew T. Athon, Travis Tenner, and Luther W. McDonald IV*

Cite This: *ACS Omega* 2023, 8, 16896−16906

Read Online

ACCESS | Metrics & More | Article Recommendations | Supporting Information

ABSTRACT: The surface morphology characteristics of post-enrichment deconversion products in the nuclear fuel cycle are important for producing nuclear fuel pellets. They also provide the first opportunity for a microstructural signature after conversion to gaseous uranium hexafluoride (UF_6). This work synthesizes uranium oxides from uranyl fluoride (UO_2F_2) starting solutions by the wet ammonium diuranate route and a modification of the dry route. Products are reduced under a nitrogen/hydrogen atmosphere, with and without water vapor in the reducing environment. The crystal structures of the starting materials and resulting uranium oxides are characterized by powder X-ray diffraction. Scanning electron microscopy (SEM) and focused ion beam SEM with energy-dispersive X-ray spectroscopy (EDX) are used to investigate microstructural properties and quantify fluorine impurity concentrations. Heterogeneous distributions of fluorine with unique morphology characteristics were identified by backscatter electron imaging and EDX; these regions had elevated concentrations of fluorine impurities relating to the incomplete reduction of UO_2F_2 to UO_2 and may provide a novel nuclear forensics morphology signature for nuclear fuel and U metal precursors.

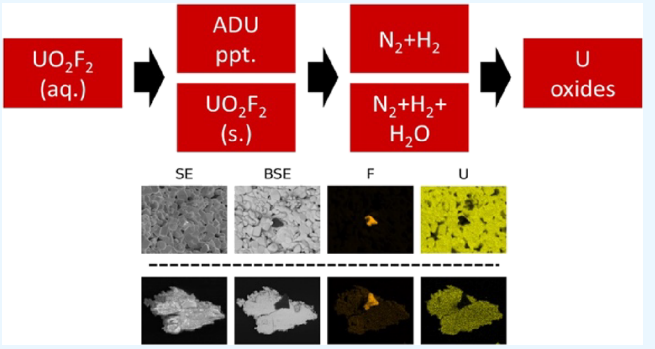

INTRODUCTION

Following the conversion of refined uranium oxides to gaseous uranium hexafluoride, UF_6, and isotopic enrichment for use in nuclear reactors or nuclear weapons, uranium (U) is recovered by "wet" or "dry" deconversion synthesis pathways before being further processed into the final desired product.[1] Wet deconversion involves first dissolving UF_6 into water to form a uranyl fluoride, UO_2F_2, solution.[2,3] The wet ammonium diuranate (ADU) route recovers U by the precipitation reaction resulting from the addition of ammonia (NH_3) gas or ammonium hydroxide (NH_4OH) to UO_2F_2.[4−7] While commonly referred to as ADU, the actual product can be any number of compounds depending on the specific parameters used for synthesis.[6] Similarly, the wet ammonium uranyl carbonate (AUC) route precipitates U by the addition of ammonium carbonate, $(NH_4)_2CO_3$, or NH_3 with carbon dioxide, CO_2.[8,9] The dry route produces a UO_2F_2 salt by the hydrolysis reaction of UF_6 and steam.[2,10]

Each intermediate deconversion product can be converted to uranium dioxide (UO_2) by reducing in a hydrogen atmosphere at temperatures at or above 500 °C.[2,11] Materials from each route might undergo an additional high-temperature decomposition step in a nitrogen atmosphere that produces an intermediate uranium oxide before its reduction.[2,12] UO_2 powders can then be pressed and sintered into dense pellets for use in nuclear power reactors.[12] Alternatively, the UO_2 powders or unreduced UO_2F_2 can be converted to UF_4 for conversion to compounds for advanced nuclear reactor fuels or U metal, which can be used as fuel for some fast neutron power reactors and research reactor designs or nuclear weapons utilizing uranium.[13−15]

The surface morphology and fluorine impurity concentrations have long been studied for deconversion materials, particularly UO_2 fuel properties. Since high densities of UO_2 fuel pellets are desired for optimal reactor efficiency, past research has investigated the effects of chemical and thermal processes on powder particle sizes and the resulting sintered UO_2 pellet densities.[16−19] Fluorine's high reactivity can damage reactor fuel cladding and compromise the reactor's integrity. As such, standards for allowable fluorine concen-

Received: February 2, 2023
Accepted: April 13, 2023
Published: May 2, 2023

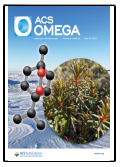

trations in fuels have been set, and methods for its removal have been devised.[16,20−22] In particular, steam during the reduction reaction is advantageous for removing fluorine.[2,20,23]

The physical and chemical properties of deconversion products are also of interest to nuclear forensics investigators, which use analytical techniques to determine the origins of unknown interdicted nuclear materials to provide evidence supporting broader law enforcement investigations. Recent work has investigated the surface morphology characteristics of UO_2 produced by the ADU and AUC routes.[24] Other works have shown the uranyl solution precipitation to play a large role in the resulting surface morphologies observed for precipitates and calcined or reduced uranium oxide products.[25,26]

Several recent works have investigated the morphological properties of UO_2F_2[27] or its chemical degradation under different environmental conditions.[28−31] Miskowiec et al. used electron microscopy with energy-dispersive X-ray spectroscopy (EDX) and nanoscale SIMS (NanoSIMS) to observe the surface morphology of dry-route UO_2F_2 that had been calcined at varying temperatures.[32] Low-temperature calcinations resulted in radiating, fibrous, and subhedral surface morphologies with higher fluorine-to-uranium (F/U) ratios measured by EDX and NanoSIMS; higher-temperature calcination products saw lower F/U ratios and only subhedral morphologies.[32] EDX point scans showed fluorine concentrations to be heterogeneous, which the authors believe could result from surface morphology features. However, no link between measured F/U ratios and local microstructural features was reported in this work.[32] We synthesize materials by the wet ADU and dry routes, resulting in distinct surface morphologies, which will be reduced under H_2 atmospheres with and without water vapor. SEM−EDX will be used to analyze materials from each route to identify and characterize heterogeneous regions of local surface microstructures and fluorine concentrations. Three-dimensional focused ion beam (FIB) tomography was recently used to measure the internal morphology of calcined and uncalcined plutonium oxalates as a potential nuclear forensics signature.[33] Here, FIB-SEM is paired with EDX to quantify F/U ratios through cross sections of materials.

MATERIALS AND METHODS

Materials Synthesis. A stock of uranium trioxide (UO_3) was prepared by rapidly adding hydrogen peroxide at a molar excess to a depleted uranium (DU) uranyl nitrate solution to precipitate uranyl peroxide. The uranyl peroxide precipitates were aged for 30 min in the precipitation vessel before recovery by vacuum filtration; the filter cakes were dried overnight at room temperature followed by additional drying at 80 °C in an atmospheric box furnace. Finally, the dried products were ground by a mortar and pestle with a small amount of *n*-pentane for more consistent grinding, then transferred to platinum crucibles, and calcined in a tube furnace at 400 °C for 8 h with a 500 mL/min flow of dry air. Precision flowmeters controlled all gas flow rates in the tube furnace.

Ammonium Diuranate Route. The starting UO_2F_2 solution for the ADU synthesis route was prepared by dissolving 0.5 g of UO_3 stock into 18.2 mL of 1% (w/v) hydrofluoric acid (Ricca Chemical). UO_3 was digested at room temperature, stirring at 400 rpm with a PTFE-coated magnetic stir bar in a closed 90 mL volume Savillex PFA jar. The resulting solution had a uranium loading of 27.4 g/L and an approximate F/U molar ratio of 6.0 to model after the dissolution of UF_6 in water. A 2.5 M NH_4OH precipitant solution was prepared from the dilution of 20% (v/v) NH_4OH (Fisher brand, TraceMetal grade) with a roughly equal volume of deionized (DI) water.

The precipitation of ADU was performed at room temperature stirring at 300 rpm in the same open PFA jar at room temperature. The precipitant was titrated into UO_2F_2 at an average rate of 0.3 mL/min with an average total volume of 3.4 mL added. Once a pH > 9 was measured with a calibrated pH electrode, titration was stopped, and the precipitate was allowed to age for 30 min under the same conditions. The precipitates were recovered by vacuum filtration glass filter frits with a 4 to 5.50 μm porosity range and were subsequently washed with five 20 mL volumes of DI water. The filter cakes were dried for a minimum of four days in a vacuum desiccation chamber with silica desiccants before removal from the filter and grinding by a mortar and pestle. Dried precipitates from the wet ADU route were decomposed to U_3O_8 by heating to 800 °C with a 16 h dwell time under a N_2 atmosphere in an alumina tube furnace.

Attempts were made to synthesize materials by the wet AUC route using the same UO_2F_2 starting solution and $(NH_4)_2CO_3$ precipitants of various concentrations. While some material was recovered, the yields were low and inconsistent. More details on the AUC precipitation attempts can be found in the supplementary material.

Uranyl Fluoride Dry Route. UO_2F_2 salts were produced by the evaporation of UO_2F_2 solutions. The starting solution for the dry synthesis route was prepared by dissolving 0.5 g of UO_3 into 7.6 mL of 1% HF while stirring in a closed PFA jar at room temperature. Once fully dissolved, the PFA closure was replaced with a PFA cap containing two 1/8″ openings. One opening was connected to a small electric aquarium pump by Teflon tubing, and the other was connected to a PFA impinger filled with a sodium hydroxide (NaOH) solution. The vessel containing the UO_2F_2 solution was heated at 50 °C on a hot plate while a gentle flow of air was passed through the vessel to remove HF fumes that were bubbled through NaOH for neutralization. After heating for 9−10 h, the solution had completely evaporated, and the PFA jar was removed from the hot plate to further dry in a vacuum desiccation chamber for 5−6 days. The dried salt was then ground by a mortar and pestle until a fine powder was achieved.

All materials synthesis was performed in a fume hood. All materials were stored in a vacuum desiccation chamber between synthesis steps until they were removed for further analysis.

Reduction. Hydrogen reductions were then performed with and without water vapor for the decomposed ADU products and dried UO_2F_2 salts. For either reduction, the alumina tube furnace was ramped to 550 °C at 5 °C/min under a N_2 atmosphere with a flow rate of 100 mL/min. Upon reaching the set point, the gas flow was switched to 440 mL/min of a 90% N_2 balance H_2 tank with an additional 60 mL/min flow of N_2 from a separate tank. After a 5 h dwell time, the flow was switched to 500 mL/min of N_2 only for 30 min before the temperature began to ramp down to room temperature under a N_2 environment. Sample masses of 160 and 200 mg were aliquoted into platinum crucibles for the decomposed ADU and dry-route products, respectively.

https://doi.org/10.1021/acsomega.3c00699
ACS Omega 2023, 8, 16896−16906

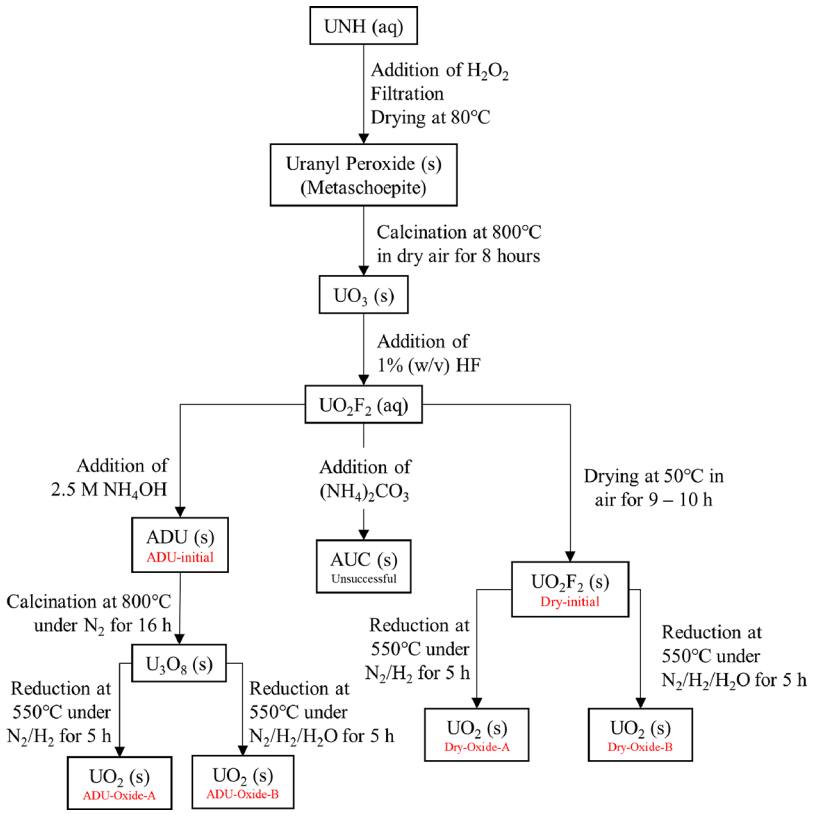

Figure 1. Flowchart describing the synthesis and naming schemes of samples used in this study.

Figure 1 and Table S1 help describe the synthesis steps and naming schemes presented in this work. ADU precipitates and dried UO_2F_2 salts are referred to as "ADU-initial" and "dry-initial", respectively. Products reduced under the N_2/H_2 atmosphere are referred to as "ADU-oxide-A" or "dry-oxide-A", and products reduced under the $N_2/H_2/H_2O$ atmosphere are referred to as "ADU-oxide-B" or "dry-oxide-B".

For the reduction in the presence of water vapor, the same 440 mL/min flowrate from the 90% N_2 balance H_2 tank was used, but the 60 mL/min flow of N_2 was passed through a volume of DI water using the apparatus described by Klosterman et al. before entering the tube furnace.[34] Previous experiments determined 60 mL/min to be the point at which the N_2 flowing through the submerged membrane became saturated. The water vapor concentration was previously measured at the tube furnace outlet by a Picarro L2130-i isotope and gas concentration analyzer. The mean water vapor content in 50 mL/min N_2+H_2O was 440 mL/min. N_2 dilution flow was determined to be 5240 ± 40 ppm by 2165 cavity ring-down spectroscopy (CRDS) measurements taken over the course of 30 min. The water vapor content was calculated to be 6290 ± 50 ppm H_2O when adjusted for the actual flow rate of 60 mL/min used during the reductions.

Analytical Techniques. Powder X-ray diffraction (P-XRD) analysis was used to determine the crystal structure of the intermediate and final products of each synthesis route. A Bruker D2 Phaser diffractometer with a 5.41874 Å Cu Kα X-ray source running at 30 kV and 10 mA was used for characterization. The beam optics used included a 0.6 mm divergence slit, a 1 mm antiscattering beam knife, and a 3 mm receiving slit. Scans were taken over the 10 to 70° 2θ range with step sizes of 0.02° 2θ with step times of 1 s/step with the sample stage rotating at 15 rpm. Roughly 50−70 mg of powder samples was loaded onto zero background silicon crystal sample holders; additional sample grinding was performed if the initial signal-to-noise ratio of a scan was poor. Match! version 3 software was used for pattern preprocessing and phase identification. Rietveld refinement for quantifying the identified phases was performed using the FullProf program with default settings.

Samples were prepared for SEM−EDX by dusting <5 mg of powder onto conductive carbon tape on aluminum pin stubs. The SEM stubs were lightly tapped to remove loose particles before analysis. An FEI Teneo field emission scanning electron microscope was used to acquire micrographs using the T1 and T2 detectors for backscatter electrons (BSE) and secondary electrons (SE), respectively. Charging effects were present in some micrographs, even when samples were sputter coated with about 20.0 nm of gold/palladium; only uncoated samples were included for elemental analyses.

An EDAX Octane Elite solid-state detector (SSD) was used for EDX scans while simultaneously imaging with an Everhart−Thornley detector (ETD) for SE and T1 detectors for BSE. Beam voltages of 8−10 kV were used for EDX analysis. Spectra for the ADU precipitates and dry-route UO_2F_2 products were acquired over 6.5 min, while longer 14.5 min scans were used to analyze the reduced materials, enabling fluorine detection at lower concentrations. The EDAX APEX software suite was used for EDX data collection and elemental quantification.

Cross-sectional imaging by FIB-SEM was used to investigate the apparent discrepancy in fluorine impurity concentrations on reduced dry-route materials by bulk analysis (P-XRD) and surface analysis (EDX). Cross-sectional imaging was performed with an FEI Helios Nanolab 650 SEM equipped with a gallium-based focused ion beam (FIB). The mounted samples

https://doi.org/10.1021/acsomega.3c00699
ACS Omega 2023, 8, 16896−16906

were first imaged, and EDS was performed using the TEAM EDS software suite. Then, the FIB was used to mill in 100 nm increments into the sample followed by imaging and EDS after each successive mill. Ion milling was performed at a 30 kV beam energy and a 40 nA ion current.

Morphological Analysis of Materials (MAMA) particle segmentation software was used for quantitative morphology analysis of microparticles from the reduced ADU route materials following the criteria defined by Olsen et al.[35] Micrographs for segmentation were acquired by a Teneo T2 SE detector using a horizontal field width (HFW, the physical distance represented horizontally across the image) of 55.3 μm.

RESULTS AND DISCUSSION

The wet ADU route precipitation reactions formed a vibrant yellow precipitate that fell out of solution near a neutral pH. Precipitates were easily filtered and washed, with an average filtration rate of about 10 mL/min for the initial precipitant volume and the subsequent DI water wash volumes. The filtrate was visually clear. After drying and grinding, 0.495 ± 0.040 g of the precipitate was recovered for each experimental replicate for an average yield of 88 ± 7%. Decomposition of the dried ADU route precipitates at 800 °C for 20 h under a N_2 atmosphere caused a mass change of −14.33 ± 0.05%; the color changed from vibrant yellow to black during the high-temperature decomposition. Reducing in a N_2/H_2 atmosphere with and without steam saw mass changes of −0.57 ± 0.05 and −0.45 ± 0.07%, respectively. No color change was observed upon reducing the ADU route materials.

The dry-route UO_2F_2 solutions required between 8.5 and 10.0 h to fully evaporate on the hot plate at 50 °C. The UO_2F_2 salts were initially translucent yellow green. Upon drying for several days in a vacuum desiccation chamber, the materials changed in color to opaque pale yellow. The dry-route material reduced without water vapor underwent a mass change of −9.59 ± 0.07%, converting to a granular olive-green powder that partially stuck to the platinum crucible, requiring some scraping with a spatula for removal. The dry-route starting materials reduced in the presence of water vapor saw a mass change of −19.2 ± 0.7% and a color change from pale yellow to dark brown.

P-XRD. Powder X-ray diffraction patterns collected for the dried ADU route starting material and reduced materials are shown in Figure 2. The dried precipitates (Figure 2a) were matched to powder diffraction file (PDF) no. 00-044-0069 from the International Centre for Diffraction Data (ICDD) database.[36] This reference pattern corresponds to uranium amine oxide hydrate, $U_2(NH_3)O_6{\cdot}3H_2O$, a common product from the precipitation reactions of uranyl solutions and ammonia.[24,34,37,38] The P-XRD patterns collected for the ADU route materials reduced in a N_2/H_2 atmosphere (Figure 2b) and a $N_2/H_2/H_2O$ atmosphere (Figure 2c) showed no differences qualitatively. Crystalline phases in the reduced materials were matched to reference patterns in the Crystallography Open Database (COD). U_3O_8 (ref. 96-231-0520) and U_4O_9 (ref. 96-231-0340) phases were identified.[39−41] No UO_2 phases could be identified in the P-XRD patterns of the reduced ADU route materials (ADU-A and ADU-B). Low intensity peaks at 15.87° 2θ were seen in the P-XRD patterns for several reduced ADU route oxides, but a suitable candidate phase could not be identified.

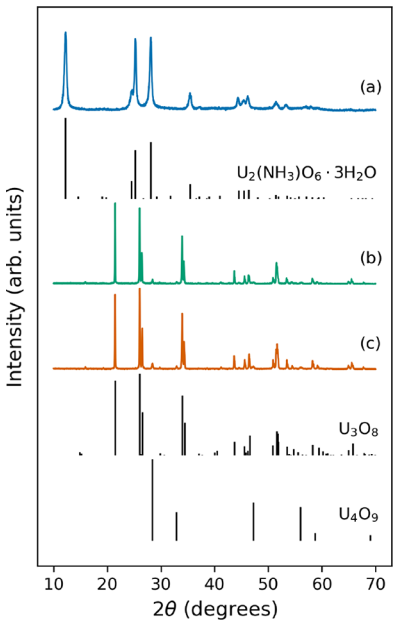

Figure 2. P-XRD patterns and reference patterns for (a) ADU-initial, (b) ADU-oxide-A, and (c) ADU-oxide-B.

Rietveld refinement analysis performed on the P-XRD patterns of the ADU route materials (Table 1) reveals that

Table 1. Results of Phase Quantification by Rietveld Refinement Analysis for Reduced Materials from the Wet ADU Synthesis Route[a]

	crystalline phase, mean wt % ± 1σ	
sample	U_3O_8	U_4O_9
ADU-oxide-A	93.0 ± 1.4%	7.0 ± 1.4%
ADU-oxide-B	92.4 ± 2.3%	7.6 ± 2.3%

[a]Peaks at 15.87° 2θ in the patterns for several replicates indicates the presence of a third phase that could not be identified.

U_3O_8 is the most predominant crystalline phase, making up >90 wt % for the oxides reduced with and without water vapor present. The quantified phases for each reducing atmosphere were the same within 1σ uncertainty. Dwell times of 5 h have previously been sufficient for reducing uranium oxides to UO_2 in a H_2 atmosphere.[24,34,42,43] However, this work marks the authors' first attempts at reductions using a premixed 90% N_2 + 10% H_2 gas cylinder, rather than separate pure H_2 and N_2 or He for dilution; this suggests that longer conversion times at temperature will be required for fully reducing UO_3 and U_3O_8 powders to U_4O_9 or UO_2 with this specific furnace system.

The dry-route starting materials were identified by P-XRD analysis as $[(UO_2F_2)(H_2O)]_7{\cdot}4H_2O$, uranyl fluoride sesquihydrate, matching to reference pattern 96-153-2890 from COD (Figure 3a).[44] The crystal structure of the dry-route material produced by evaporation was the same as those produced by the hydrolysis reaction of UF_6 (g) with steam in several recent publications.[28−30]

Figure 3 shows a representative P-XRD pattern of the dry-initial product reduced in an environment without water vapor present (dry-oxide-A), which contained anhydrous UO_2F_2 (COD ref. 96-900-9153), U_3O_8 (COD ref. 96-231-0520), and minor UO_2 (COD ref. 96-154-1666) phases.[39,41,45] Quantification of the crystalline phases identified anhydrous

https://doi.org/10.1021/acsomega.3c00699
ACS Omega 2023, 8, 16896−16906

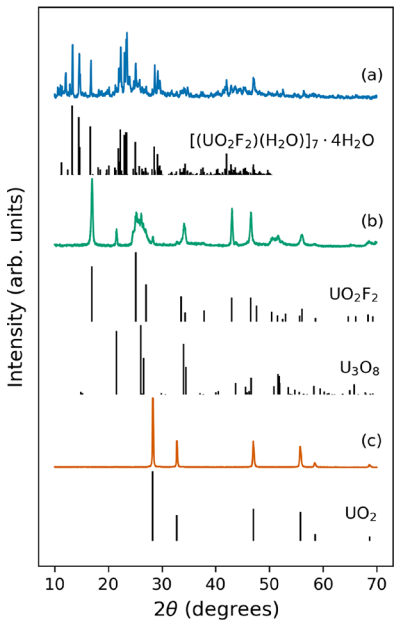

Figure 3. P-XRD patterns and reference patterns for (a) dry-initial, (b) dry-oxide-A, and (c) dry-oxide-B.

UO_2F_2 as the predominant phase at an average proportion of 71.0 ± 6.0 wt % across three experimental replicates (Table 2). U_3O_8 (27.2 ± 5.4 wt %) was the second most prevalent phase, with UO_2 making up the balance. Overlapping UO_2F_2 and U_3O_8 peaks in the 24−28 and 49−53° 2θ ranges were seen in these P-XRD patterns.

Fulconis et al. saw slow kinetics in reducing UO_2F_2 hydrates to UO_2 in a dry hydrogen atmosphere, requiring approximately 100 h to fully convert.[11] Previous studies have attributed the slower conversion rate in the absence of water vapor to the formation of a UF_4 layer, which inhibits the reduction reaction.[2,10,23] Chemical analyses by Federer et al. identified UF_4 phases with up to 20% abundance in UO_2F_2 reduction products under certain conditions for the reduction reactions, though no details were given to the characterization methodologies; their P-XRD analyses did not identify UF_4 crystalline phases for all samples, and UF_4 phases had relatively weak intensities when identified.[10] Further studies will be required to characterize the formation and abundance of UF_4 layers in UO_2F_2 reduction products.

For dry-oxide-B, 2/3 of the dry-route replicates underwent near complete (>99 wt %) conversion to UO_2 as determined by Rietveld refinement analysis (Figure 3c and Table 2). The remaining replicate showed equal fractions of U_3O_8 and U_4O_9 phases, at 38.0 ± 1.2 and 38.2 ± 2.4 wt %, respectively, with 23.8 ± 2.0 wt % UO_2 (Figure S12). Each replicate of dry-route starting material reduced with water vapor present was analyzed by SEM/EDX.

Rietveld refinement phase percentages, *R*-factors, and goodness of fit metrics can be found in Tables S2−S4 for all reduced materials.

Surface Morphology. The Tamasi et al. lexicon "for the consistent description of material images for nuclear forensics" was applied to qualitatively describe micrographs from each processing route.[46] Keywords from the lexicon are emphasized by italic typeface.

Ammonium Diuranate Route. Figure 4 shows a representative BSE micrograph for ADU-initial after drying and

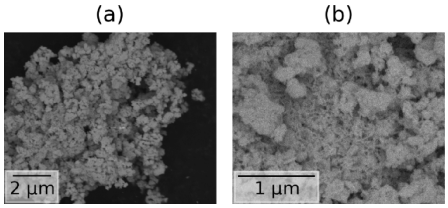

Figure 4. (a,b) BSE micrographs of ADU-initial particles showing the bimodal distribution of subrounded grains and columnar acicular grains.

mounting for SEM analysis. The wet ADU route precipitates can be best described as having the material nature of complex particles, showing agglomerates of subrounded and columnar subparticles/grains in irregular spatial grouping. The subrounded grains in the bimodal conglomerate showed medium sphericity and irregular shapes with a somewhat rough surface texture. The columnar particles are best described as acicular and smooth.

Upon decomposition at 800 °C in N_2 gas and subsequent reduction, the ADU route materials underwent significant changes in surface morphology. Qualitatively, the surface morphology of the reduced ADU route materials from either route is identical (Figure 5). As with the ADU precipitates,

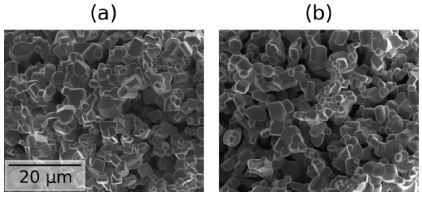

Figure 5. SE micrographs of (a) ADU-oxide-A and (b) ADU-oxide-B; bimodal conglomerates with larger grains displaying subhedral growth and smaller well-rounded grains can be seen for each.

complex particles as bimodal agglomerates are seen, though macroparticles exhibited a rounded/subrounded and tabular appearance (Figure S15). The smaller grains in the bimodal agglomerates were well-rounded, spherical, and smooth, exhibiting the characteristics of sintered materials. The larger

Table 2. Results of Phase Quantification by Rietveld Refinement Analysis for Reduced Materials from the Dry Uranyl Fluoride Synthesis Route[a]

	crystalline phase, mean wt % ± 1σ			
sample	UO_2F_2	U_3O_8	U_4O_9	UO_2
dry-oxide-A	71.0 ± 6.0%	27.2 ± 5.4%		1.7 ± 0.7%
dry-oxide-B		12.9 ± 17.7%	12.7 ± 18.0%	74.4 ± 35.8%

[a]Excluding replicate no. 1: 0.3 ± 0.3% U_3O_8, 99.7 ± 0.3% UO_2.

https://doi.org/10.1021/acsomega.3c00699
ACS Omega 2023, 8, 16896−16906

grains are faceted and show subhedral growth, meaning that some of the crystal faces developed on their own and some formed against the faces of other grains in crowded growth.[46] The more faceted larger grains were roughly equiaxed and hexagonal with a smooth texture.

MAMA software was used to segment and quantify 908 unique particles from the ADU material reduced without steam and 917 particles from the material reduced with steam. Kernel density estimates for pixel area, perimeter, circularity, and ellipse aspect ratio features can be seen in Figure 6 for each ADU-oxide sample.

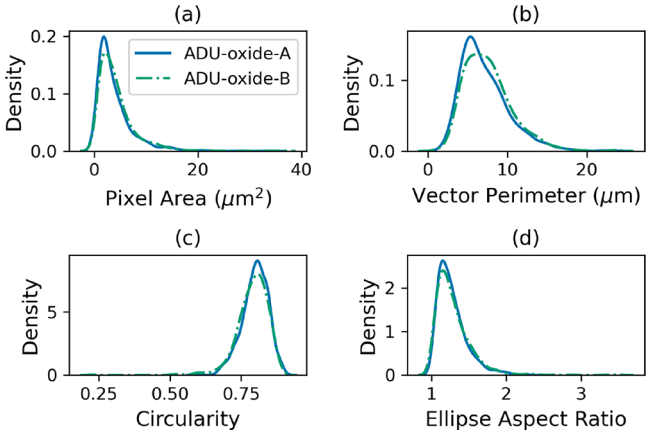

Figure 6. Comparison of quantitative morphology features for reduced ADU. (a) Pixel area and (b) vector perimeter provide complementary information regarding the size of segmented particles. (c) Circularity and (d) ellipse aspect ratio features provide complementary information about the roundness and elongation of segmented particles.

The pixel area feature shows a long right tail and a slight peak after 10 μm^2 for each set of quantified particles, corresponding to the bimodal distribution described; the lower relative density of larger particles compared to what was seen qualitatively is a result of larger particles' edges having a higher likelihood of being partially obscured by smaller particles. The median pixel areas were 2.78 (inner quartile range, IQR, 1.64−4.96) and 3.28 μm^2 (IQR, 1.84−5.31) for ADU-oxide-A and ADU-oxide-B, respectively (Table S5), indicating that the materials reduced with steam were slightly larger. U_3O_8 and UO_2 synthesized from ADU precipitated from uranyl nitrate solutions by Schwerdt et al. respectively had median pixel area values of 0.030 and 0.025 μm^2, meaning that the reduced ADU-route oxides from uranyl fluoride solutions were two orders of magnitude larger than those from uranyl nitrate solutions.[24] A process patent awarded to Yato et al. suggests that the larger particle sizes of UO_2 precipitated as ADU from UO_2F_2 solutions are due to NH_4F coprecipitates leading to greater powder agglomeration. However, further investigation of this phenomenology was outside the scope of this work.[47]

Kernel density estimate plots for shape features (circularity and ellipse aspect ratio) quantified by particle segmentation showed little difference in the distributions of ADU-route oxides from either reducing environment. This was confirmed by a two-sample Kolmogorov−Smirnov (KS) test.[48] At a 95% confidence interval (CI), the circularity feature distributions required 500 segmented particles per route to reject the null hypothesis; the null hypothesis for the ellipse aspect ratio could not be rejected with even the full set of segmented particles, meaning that the samples were drawn from the same distribution. In contrast, the pixel area and vector perimeter features only required 250 particles to reject the null hypothesis at a 95% CI (Table S6).

Uranyl Fluoride Dry Route. Dry-initial materials had the nature of complex particles that are polydisperse, with widths ranging from several micrometers to over 100 μm. Particles were blocky with angular edges; many particles had a flattened disc shape, as demonstrated by Figure 7, though some particles

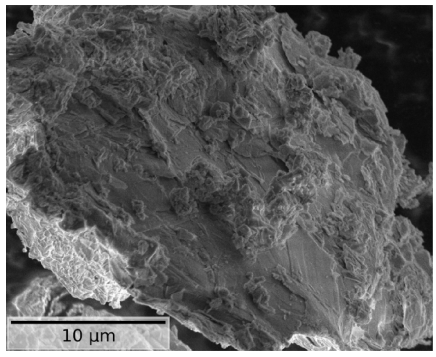

Figure 7. BSE micrograph of UO_2F_2 hydrates from the dry synthesis route showing large platelets with varied surface decorations.

had more irregular or blocky shapes. Overall, the larger substructure of the complex particles had a somewhat smooth to somewhat rough texture. However, a wide variety of surface decorations could be identified, including pits/pores, rippled surface patterns, broken crusts and fines adhering to the surface, and cracks (Figure S16). The characteristics and distribution of surface decoration features on the individual particles were heterogeneous, varying greatly from particle to particle and often locally across the same particle. Sharp, angular textures around particle edges indicate that the samples had been crushed prior to imaging.

Furthermore, the surface morphology seen by UO_2F_2 produced by evaporation of the starting solution shows distinct surface morphologies from UO_2F_2 synthesized by the hydrolysis of UF_6 with water vapor, as reported in the literature. Kirkegaard et al. presented UO_2F_2 salts with a subhedral/blocky morphology when freshly synthesized or aged in humid environments for shorter times and a fibrous/irregular morphology when aged for longer periods.[30] Kips et al. showed drastically different UO_2F_2 surface morphologies producing somewhat spherical single particles that were submicrometer in size, though some clustering/agglomeration occurred under certain synthesis conditions.[27]

Reduction of the dry-route materials under either condition led to similar surface morphology features to the starting UO_2F_2 material, with no changes to the overall particle shape. Experience with the calcination and reduction of larger, porous AUC particles would suggest a possible change in size, shape, and distribution of pores and cracks across the surface.[24] However, the presence and characteristics of pores remained varied and heterogeneous across the unreduced and reduced materials.

Figure 8 shows BSE images representing the diversity of surface decorations across dry-oxide-B materials. The top left micrograph shows a surface that is relatively nonporous, though relatively small pores can be seen on some of the

https://doi.org/10.1021/acsomega.3c00699
ACS Omega 2023, 8, 16896−16906

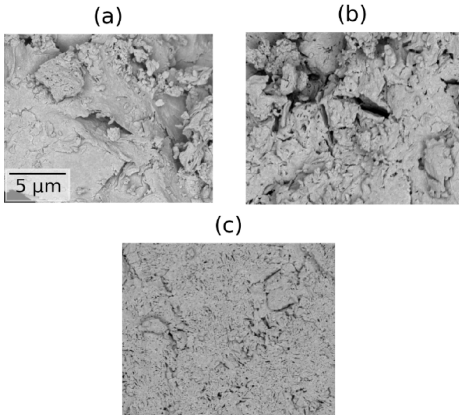

Figure 8. BSE micrographs demonstrating (a) nonporous, (b) sparsely distributed large pores, and (c) densely distributed pores for dry-oxide-B.

subparticles. Larger and more sparsely distributed pores and cracks can be seen in the top right, and smaller pores with tighter clustering can be seen in the bottom micrograph. There were no apparent differences between the replicates that had fully reduced to UO_2 and the replicate that had incomplete conversion. Similar morphological trends were seen for dry-initial (Figure S17) and dry-oxide-A (Figure S18). The diversity of morphology features seen within single replicates across each of the reducing conditions indicates that the surface morphology alone is not particularly useful to identify the conditions used to reduce UO_2F_2.

Fluorine Impurity Concentrations. Bulk EDX techniques were used to quantify the fluorine-to-uranium (F/U) atomic ratio for each synthesis route (Figure 9). Tables S7–S13 contain additional information from the EDX scans, including minimum detection limits.

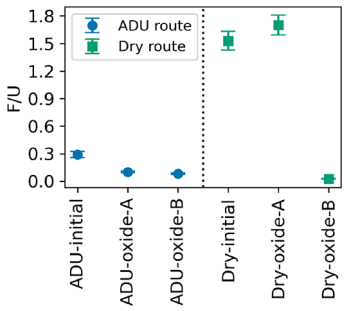

Figure 9. Comparison of mean fluorine/uranium ratios measured by EDX scans for each synthesis route; error bars represent the 95% confidence interval.

ADU-initial precipitates were quantified to have an F/U of 0.292 ± 0.020 (1σ). ADU-oxide-A had a fluorine content of 0.101 ± 0.005, roughly a factor of three lower than what was measured for the precipitates. ADU-oxide-B saw an additional decrease in fluorine content to 0.081 ± 0.004. At a 95% confidence interval, the F/U ratios of the two ADU reduction environments do not show statistical significance by the one-way analysis of variance test (ANOVA).

Dry-initial samples had an F/U ratio of 1.53 ± 0.05; dry-oxide-A had an F/U ratio of 1.70 ± 0.06. When dry-route materials were reduced in the presence of water vapor, dry-oxide-B had an F/U of 0.026 ± 0.004. This represents a 60-fold decrease in fluorine content from the unreduced material and a lower fluorine content than any of the ADU route materials. Despite the reduced dry routes having relatively large differences in fluorine impurity concentrations and completely different mixes of crystalline phases, the surface morphologies from the two pathways remained remarkably similar to the starting hydrated UO_2F_2 and between the reduction pathways.

Fluorine concentrations were homogeneous across all mapping scans taken of the ADU-initial materials, and no low-atomic-mass regions were identified in the corresponding BSE micrographs of these materials (Figure S19). While reduced ADU route materials were homogeneous for most EDX scans, there were several instances in which low-Z regions could be identified and analyzed; these regions were seen with similar frequencies in both sets of reduced materials from the ADU route.

Figure 10 presents SE and BSE images and uranium and fluorine EDX maps for one such region identified in ADU-

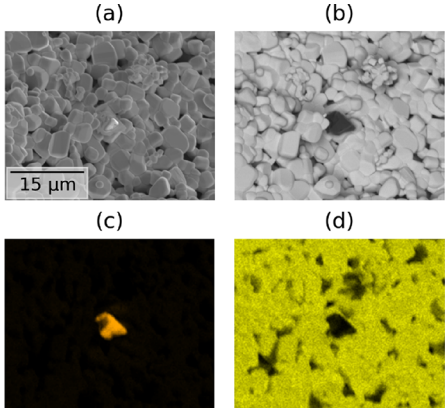

Figure 10. (a) Secondary electron and (b) backscatter electron micrographs and EDX maps for (c) fluorine and (d) uranium of a region containing a high fluorine concentration for a subsample of ADU-oxide-B. EDX scans and micrographs were acquired with a beam voltage of 10 kV, a spot size of 10, and a working distance of 9.6 mm.

oxide-B. In the center of the BSE micrograph (Figure 10b), a dark region roughly 5 μm by 5 μm in size is seen partially obscured by other subparticles in the image; the corresponding particle on the SE micrograph (top left) can be seen with charging effects that are not seen for other particles. Whereas the surface morphology of the nonanomalous subparticles is either well-rounded/spherical or faceted/subhedral hexagonal as previously defined, the high fluorine concentration anomaly appears faceted and flattened. Elemental quantification of the entire image region measures 4.4 ± 0.4 at. % F and 15.8 ± 0.6 at. % U. A reduced region centered on this high fluorine region was quantified as 44.1 ± 3.8 at. % F and 11.8 ± 0.5 at. % U. The 3.5 ± 0.3 F/U ratio at this region of interest (ROI) could indicate the formation of UF_4. Additional EDX mapping data for ADU route materials reduced without steam and with steam can be seen in Figures S20 and S21, respectively.

Regions with elevated fluorine concentrations were identified for dry-initial, dry-oxide-A, and dry-oxide-B samples. For dry-initial, fluorine was concentrated in individual flattened platelets with widths in the range of 5 to 10 μm. One such ROI can be seen in Figure 11. Quantification of the EDX spectrum corresponding to only the ROI shows a relatively high F/U

https://doi.org/10.1021/acsomega.3c00699
ACS Omega 2023, 8, 16896−16906

ratio of 14.0 ± 1.5; the entire scan region was quantified with an F/U of 3.2 ± 0.3.

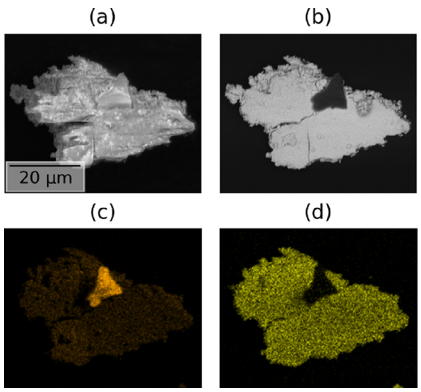

Figure 11. (a) Secondary electron and (b) backscatter electron micrographs and EDX maps for (c) fluorine and (d) uranium of a particle containing a high fluorine concentration subparticle from a dry-initial replicate. EDX scans and micrographs were acquired with a beam voltage of 10 kV, a spot size of 10, and a working distance of 10.0 mm.

The flattened oblate particle shown in Figure 12 was imaged on a dry-oxide-B replicate. Its width is about 5 μm, which is

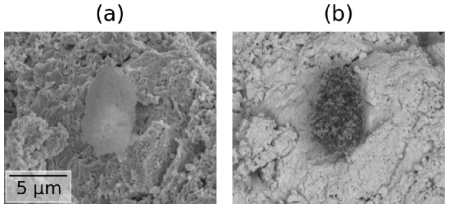

Figure 12. (a) Secondary electron and (b) backscatter electron micrographs of a flattened oblate subparticle on the surface of a UO_2 particle from dry-oxide-B.

similar in size to the high fluorine regions identified in the unreduced dry-route materials. Unlike the unreduced material, this subparticle exhibits signs of pores and a rough texture. As imaged by backscatter electrons (Figure 12b), the subparticle appears speckled with submicrometer high-Z regions, possibly indicating a lower concentration of fluorine than the unreduced materials. Quantification of this region on the EDX maps indicated an F/U ratio of 1.2 ± 0.2, an order of magnitude lower than the region of unreduced material quantified in Figure 10. The EDX spectrum and maps for this particle can be seen in Figure S22.

The exact chemical composition of these heterogeneous regions with high fluorine-to-uranium ratios remains uncertain. As measured by EDX for local regions, the concentrations varied greatly, ranging from F/U ≈ 14 to F/U ≈ 1. The reason for this is two-fold. First, EDX is known to perform best when sample surfaces are flat and smooth, possibly having undergone some degree of grinding and polishing before analysis. The nature of the irregular powder samples presented in this work is not optimal for elemental analysis by EDX as the complex topographies often cause reabsorption of characteristic X-rays from ROIs in the direction of the detector.

Second, the nature of sampling heterogeneous regions lends itself to poor statistics. Dusting powders onto carbon tape for SEM analysis does little to disperse the fines from bulk particles and subparticles from agglomerates such that more individual particles can be analyzed. Future work might implement methods like ultrasonication for sample mounting to break apart agglomerates so that more heterogeneous regions can be identified and measured, thus improving the statistics.

Cross-Sectional Measurements. While the P-XRD scan and Rietveld refinement analysis quantified the U_3O_8 phase of the N_2/H_2-reduced UO_2F_2 at around 25 wt %, the bulk EDX scans do not show a decrease in fluorine content. The formation of UF_4 at the surface of the particles and the relatively narrow depths at which characteristic X-rays are generated by electrons during EDX analysis (submicrometer for 10 kV) might provide a possible explanation for this phenomenon.[49] Ogata et al. studied the kinetics of the UO_2-UO_2F_2 system for the fluorination of uranium dioxide by fluorine gas and its diffusion through the particle to better develop the FLUOREX process; results for this study came primarily from thermogravimetric analyses.[50]

To the authors' knowledge, the fluorine content across particle cross sections for UO_2-UO_2F_2 materials has not been measured for either the reduction or fluorination reaction. The authors hypothesize that FIB-SEM paired with EDX scans taken of particle cross sections will reveal a heterogeneous distribution of fluorine concentrated at the particles' surfaces in N_2/H_2-reduced materials and that $N_2/H_2/H_2O$-reduced materials will show more complete and homogeneous fluorine removal.

The interior of milled particles from dry-oxide-A and dry-oxide-B qualitatively had different morphological characteristics (Figure 13). Upon milling, the texture of the dry-oxide-B

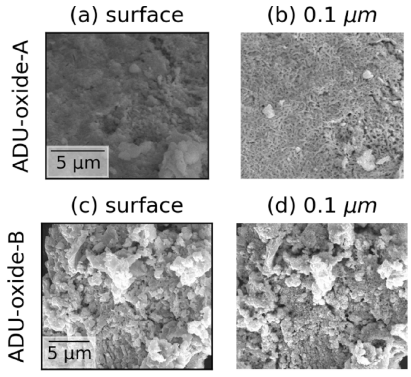

Figure 13. Micrographs of an FIB-milled particle from (a,b) dry-oxide-A and (c,d) dry-oxide-B.

was consistent at the interior cross sections and unmilled surfaces (Figure 13c,d). Dry-oxide-A samples initially had a very similar morphology (Figure 13a) to the dry-oxide-B. However, once milled, the particles showed a unique complex fibrous morphology with significant pore space in between (Figure 13b). Additional images of milled particles can be seen for dry-oxide-A and dry-oxide-B in Figures S23 and S24.

Results of the EDX scans at the milling surface can be seen in Figure 14. The F/U ratio of the dry-oxide-B remained below 0.10 across all milling depths down to 0.3 μm. The fluorine content of dry-oxide-A was initially much higher at the surface and a depth of 0.1 μm (F/U ≈ 0.6). Beyond 0.1 μm, the F/U ratio rapidly decreased, stabilizing at a fluorine content like that of the steam-reduced materials, supporting the proposed hypothesis.

https://doi.org/10.1021/acsomega.3c00699
ACS Omega 2023, 8, 16896−16906

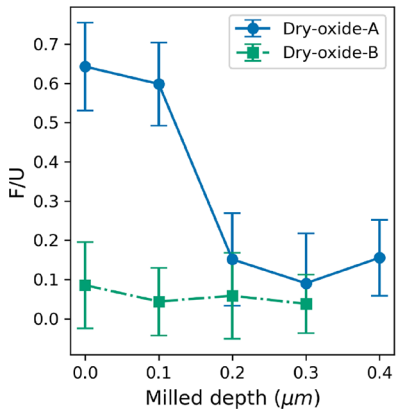

Figure 14. EDX F/U ratios for dry-route materials milled to depths up to 0.4 μm by FIB-SEM; error bars represent the 95% confidence interval.

The relatively high costs of FIB-SEM analysis limited this analysis to only a few representative particles from each reduction pathway for the dry-route materials. Nevertheless, interesting trends were observed that indicate that FIB-SEM with EDX could be a useful nuclear forensics tool for identifying the reduction conditions of dry-route UO_2F_2 materials during conversion to UO_2. The submicrometer UO_2F_2 spheres produced by the hydrolysis of gaseous UF_6 would provide more particles per unit mass and more consistent particle morphologies that would be beneficial for obtaining better statistics for the EDX analysis of FIB milled particles, which will be needed to fully develop this technique.

While EDX was useful to measure fluorine impurities, complementary microanalytical techniques, such as micro-Raman spectroscopy, will be needed identify the initial and intermediate chemical structures of the high fluorine inhomogeneous regions and any subsequent changes to these compounds upon aging.[51,52] Future work should develop an experimental design to model how varying the reducing conditions (time, temperature, furnace ramp rates, water vapor content, and H_2 content) impacts full conversion to UO_2 and fluorine removal.

CONCLUSIONS

Products resembling nuclear fuel precursors from deconversion processes were synthesized by the wet ammonium diuranate route and a modification of the dry route. P-XRD analysis identified precipitates from the ADU route as uranium amine oxide hydrate, $U_2(NH_3)O_6{\cdot}3H_2O$. The precipitates exhibited a clumped agglomerated surface morphology, consisting of a bimodal distribution with subrounded and columnar acicular grains. Upon reducing decomposed ADU route materials in a N_2/H_2 or $N_2/H_2/H_2O$ atmosphere, oxides comprising U_3O_8 and U_4O_9 phases were produced. The surface morphologies of the reduced ADU route oxides from either reducing atmosphere were bimodal clumped agglomerates with well-rounded grains and faceted subhedral hexagonal subparticles; particle size distributions from either reduction were shown to be statistically different with a 95% CI. Regions that were heterogeneous for the fluorine content were identified by BSE microscopy and EDX; fluorine was concentrated in flattened platy subparticles.

Reduction of the uranyl fluoride dry-route starting material formed a product that was primarily anhydrous UO_2F_2 and U_3O_8, as confirmed by P-XRD and Rietveld refinement analysis. In contrast, the same starting material reduced with steam present saw near complete conversion to UO_2, reiterating the importance of water vapor for fluorine removal. Low-Z regions identified in the backscatter electron micrographs of reduced dry-route materials indicate that fluorine removal may be heterogeneous even when conversion to UO_2 is nearly complete. To better understand the mechanism of fluorine removal and the formation and removal of intermediate products, additional research efforts are needed.

Surface morphologies for each dry-route material were remarkably similar, showing somewhat smooth complex particles with crusts, fines, cracks, and pores; the characteristics of porous regions varied greatly in size, shape, and density, even within the same bulk particle and experimental replicate. EDX measurements at the surface of dry-route materials reduced without steam showed F/U ratios equivalent to that of the unreduced materials, despite P-XRD analysis showing some conversion to oxides. Focused ion beam milling of these samples later revealed that fluorine impurities were largely concentrated at the surface, with F/U ratios converging to the steam-reduced concentrations at milled depths of 0.2 μm. The reducing atmosphere also led to distinct morphologies at the interiors of particles, which were only apparent from milling.

This study identified a previously hypothesized correlation between surface morphology features and fluorine concentrations in deconversion products from the nuclear fuel cycle. Unique features relating to the reducing atmosphere were only focused ion beam milling, further demonstrating this method's utility for the microstructural analysis of nuclear materials. Future research should further investigate and refine FIB-SEM for this purpose. Better sample preparation techniques and the inclusion of complementary microanalytical methods will be needed to obtain the statistical certainty and structural information needed to fully characterize the composition of high fluorine heterogeneous regions in ex-UO_2F_2 uranium oxides.

ASSOCIATED CONTENT

Supporting Information

The Supporting Information is available free of charge at https://pubs.acs.org/doi/10.1021/acsomega.3c00699.

Additional 30 figures and 17 tables, including additional details on the XRD patterns, observed morphologies in SEM images, and data processing (PDF)

AUTHOR INFORMATION

Corresponding Author

Luther W. McDonald IV − *Department of Civil and Environmental Engineering, Nuclear Engineering Program, University of Utah, Salt Lake City, Utah 84112, United States;* orcid.org/0000-0001-6735-5410; Email: luther.mcdonald@utah.edu

Authors

Cody A. Nizinski − *Department of Civil and Environmental Engineering, Nuclear Engineering Program, University of Utah, Salt Lake City, Utah 84112, United States; Pacific Northwest National Laboratory, Richland, Washington 99352, United States*

https://doi.org/10.1021/acsomega.3c00699
ACS Omega 2023, 8, 16896−16906

Jacob Olson − *Department of Civil and Environmental Engineering, Nuclear Engineering Program, University of Utah, Salt Lake City, Utah 84112, United States*
Aaron M. Chalifoux − *Department of Civil and Environmental Engineering, Nuclear Engineering Program, University of Utah, Salt Lake City, Utah 84112, United States*
Nick Kurtyka − *Department of Civil and Environmental Engineering, Nuclear Engineering Program, University of Utah, Salt Lake City, Utah 84112, United States*
Matthew T. Athon − *Pacific Northwest National Laboratory, Richland, Washington 99352, United States*
Travis Tenner − *Los Alamos National Laboratory, Los Alamos, New Mexico 87545, United States*

Complete contact information is available at: https://pubs.acs.org/10.1021/acsomega.3c00699

Notes

The authors declare no competing financial interest.

■ ACKNOWLEDGMENTS

The materials synthesis, XRD analysis, and SEM imaging of the uranyl fluoride and ammonium diuranate products were supported by the Department of Homeland Security (DHS) under project 2016-DN-077-ARI102. The reduction of starting materials to UO_x using controlled oxygen isotope ratios in dry and wet atmospheres with support was funded by the National Technical Nuclear Forensics Center (NTNFC) within Countering Weapons of Mass Destruction (CWMD), formerly the Domestic Nuclear Detection Office (DNDO), of the Department of Homeland Security. Lastly, the quantitative morphological analysis including the 3D FIB analysis was completed using support from the Department of Energy's National Nuclear Security Administration, Office of Defense Nuclear Nonproliferation Research and Development.

■ REFERENCES

(1) Ranek, N.L.; Monette, F.A. *Evaluation of UF6-to-UO2 conversion capability at commercial nuclear fuel fabrication facilities*, (2001).
(2) Brandberg, S. G. Conversion of Uranium Hexafluoride to Uranium Dioxide. *Nucl. Technol.* **1973**, *18*, 177−184.
(3) Palheiros, F.; Gonzaga, R.; Soares, A. Comparative study of the different industrial manufacturing routes for UO2 pellet specifications through the wet process. In *International Nuclear Atlantic Conference (INAC)*; INAC: Rio de Janeiro, Brazil, 2009.
(4) Seneda, J. A.; Figueiredo, F. F.; Abrão, A.; Carvalho, F. M. S.; Frajndlich, E. U. C. Recovery of uranium from the filtrate of 'ammonium diuranate' prepared from uranium hexafluoride. *J. Alloys Compd.* **2001**, *323-324*, 838−841.
(5) Thang, D.N.; Khanh, P.D.; Khai, H.D.; van Doan, N.; Thai, T.T.H.; Vuong, P.H. *Study on precipitation of amoni diuranate - (NH4) 3U2O7 from UO2F2 - HF solution for fuel ceramic UO2 powder preparation*, (2007). http://inis.iaea.org/Search/search.aspx?orig_q=RN:40057570 (accessed January 11, 2022).
(6) Rothman, A. B.; Graczyk, D. G. Ammonium Polyuranate Precipitation from Fluoride Solutions: An Experimental Study of the UO3-HF-NH3-H2O System as Applied in UF6 Processing. *Nucl. Technol.* **2009**, *167*, 410−420.
(7) Hung, N. T.; Thuan, L. B.; Van Khoai, D.; Lee, J. Y.; Jyothi, R. K. Modeling conversion of ammonium diuranate (ADU) into uranium dioxide (UO2) powder. *J. Nucl. Mater.* **2016**, *479*, 483−488.
(8) Kan-Sen, C.; Ding-Yi, L.; Mu-Chang, S. Precipitation studies of ammonium uranyl carbonate from UO2F2 solutions. *J. Nucl. Mater.* **1989**, *165*, 171−178.
(9) Maw-Chwain, L.; Chung-Jyi, W. Conversion of UF6 to UO2: A quasi-optimization of the ammonium uranyl carbonate process. *J. Nucl. Mater.* **1991**, *185*, 190−201.
(10) Federer, J. I.; Robinson, W. C.; Patterson, F. H. 1 Federer, Conversion of UF6 to UO2 in a Flame Reactor. *Nuclear Application.* **1969**, *6*, 298−306.
(11) Fulconis, J. M.; Morato, F.; Rouquerol, F.; Fourcade, R.; Feugier, A.; Rouquerol, J. CRTA Study of the Reduction of UO2F2 into UO2 by Dry H2. *J. Therm. Anal. Calorim.* **1999**, *56*, 1443−1446.
(12) Placek, C.; North, E. Uranium Dioxide Nuclear Fuel, Industrial and Engineering Chemistry (U.S.) Formerly J. Ind. Eng. Chem. Superseded by. *Chem. Technol.* **1960**, *52*, 458−464.
(13) Wilhelm, H. A. Development of uranium metal production in America. *J. Chem. Educ.* **1960**, *37*, 56−68.
(14) Frajndlich, E.U.C.; Zorzetto, M.A.; Saliba-Silva, A.M. *Alternative route for UF6 conversion towards UF4 to produce metallic uranium*; Proceedings of the XXI International Meeting on Reduced Enrichment for Research and Test Reactors: São Paulo, Brazil, 18—23.
(15) Saliba-Silva, A. M.; Durazzo, M.; de Carvalho, E. F. U.; Riella, H. G. Fabrication of U3Si2 Powder for Fuels Used in IEA-R1 Nuclear Research Reactor. *Mater. Sci. Forum* **2008**, *591-593*, 194−199.
(16) Fuhrman, N.; Hower, L. D.; Holden, R. B. Low-Temperature Sintering of Uranium Dioxide. *J. Am. Ceram. Soc.* **1963**, *46*, 114−121.
(17) Lee, Y. W.; Yang, M. S. Characterization of HWR fuel pellets fabricated using UO2 powders from different conversion processes. *J. Nucl. Mater.* **1991**, *178*, 217−226.
(18) Ayaz, B.; Bilge, A. N. The possible usage of ex-ADU uranium dioxide fuel pellets with low-temperature sintering. *J. Nucl. Mater.* **2000**, *280*, 45−50.
(19) Ching-Tsven, H. Dry-ADU process for UO2 production. *J. Nucl. Mater.* **1992**, *199*, 61−67.
(20) Lindman, N. The kinetics of the elimination of fluorine from uranylfluoride/uraniumdioxide pellets. *J. Nucl. Mater.* **1977**, *66*, 23−36.
(21) Song, Z. X.; Huang, X. W.; Xie, Z. F.; Ge, Q. R.; Wang, R. S. Defluorination behavior and mechanism of uranium dioxide. *J. Radioanal. Nucl. Chem.* **1998**, *237*, 81−84.
(22) Morel, B.; Duperret, B. Uranium and fluorine cycles in the nuclear industry. *J. Fluorine Chem.* **2009**, *130*, 7−10.
(23) Knudsen, I.E.; Hootman, H.E.; Levitz, N.M. *A fluid-bed process for the direction conversion of uranium hexafluoride to uranium dioxide*; Argonne National Lab, 1963, DOI: 10.2172/4713414.
(24) Schwerdt, I. J.; Hawkins, C. G.; Taylor, B.; Brenkmann, A.; Martinson, S.; McDonald, L. W. Uranium oxide synthetic pathway discernment through thermal decomposition and morphological analysis. *Radiochim. Acta* **2019**, *107*, 193−205.
(25) Manna, S.; Kumar, R.; Satpati, S. K.; Roy, S. B.; Joshi, J. B. Study of the Changes in Composition of Ammonium Diuranate with Progress of Precipitation, and Study of the Properties of Ammonium Diuranate and its Subsequent Products Produced from both Uranyl Nitrate and Uranyl Fluoride Solutions, Nuclear. *Eng Technol.* **2017**, *49*, 541−548.
(26) Abbott, E. C.; O'Connor, H. E.; Nizinski, C. A.; Gibb, L. D.; Allen, E. W.; McDonald, L. W. Thermodynamic evaluation of the uranyl peroxide synthetic route on morphology. *J. Nucl. Mater.* **2022**, *561*, No. 153533.
(27) Kips, R.; Leenaers, A.; Tamborini, G.; Betti, M.; van den Berghe, S.; Wellum, R.; Taylor, P. Characterization of Uranium Particles Produced by Hydrolysis of UF6 Using SEM and SIMS. *Microsc. Microanal.* **2007**, *13*, 156−164.
(28) Kirkegaard, M. C.; Langford, J.; Steill, J.; Anderson, B.; Miskowiec, A. Vibrational Properties of Anhydrous and Partially Hydrated Uranyl Fluoride. *J. Chem. Phys.* **2017**, *146*, No. 024502.
(29) Kirkegaard, M. C.; Spano, T. L.; Ambrogio, M. W.; Niedziela, J. L.; Miskowiec, A.; Shields, A. E.; Anderson, B. B. Formation of a uranyl hydroxide hydrate via hydration of [(UO 2 F 2)(H 2 O)] 7 · 4H 2 O. *Dalton Trans.* **2019**, *48*, 13685−13698.

(30) Kirkegaard, M. C.; Ambrogio, M. W.; Miskowiec, A.; Shields, A. E.; Niedziela, J. L.; Spano, T. L.; Anderson, B. B. Characterizing the degradation of [(UO2F2)(H2O)]7 4H2O under humid conditions. *J. Nucl. Mater.* **2020**, *529*, No. 151889.
(31) Kips, R.; Pidduck, A. J.; Houlton, M. R.; Leenaers, A.; Mace, J. D.; Marie, O.; Pointurier, F.; Stefaniak, E. A.; Taylor, P. D. P.; van den Berghe, S.; van Espen, P.; van Grieken, R.; Wellum, R. Determination of fluorine in uranium oxyfluoride particles as an indicator of particle age. *Spectrochim. Acta Part B* **2009**, *64*, 199−207.
(32) Miskowiec, A.; Spano, T.; Zirakparvar, N. Improving Elemental Ratio Measurements on Uranyl Fluoride with NanoSIMS; ORNL: Oak Ridge, TN (United States), 2020. DOI: 10.2172/1606864.
(33) Chung, B. W.; Torres, R. A. Microstructural characterization of plutonium oxalate and oxide particles by three-dimensional focused ion beam tomography. *Materials* **2019**, *6*, No. 100294.
(34) Klosterman, M. R.; Oerter, E. J.; Deinhart, A. L.; Chakraborty, S.; Singleton, M. J.; McDonald, L. W. Oxygen Kinetic Isotope Effects in the Thermal Decomposition and Reduction of Ammonium Diuranate. *ACS Omega* **2021**, *6*, 30856−30864.
(35) Olsen, A. M.; Richards, B.; Schwerdt, I.; Heffernan, S.; Lusk, R.; Smith, B.; Jurrus, E.; Ruggiero, C.; McDonald, L. W. Quantifying Morphological Features of α-U3O8 with Image Analysis for Nuclear Forensics. *Anal. Chem.* **2017**, *89*, 3177−3183.
(36) Debets, P. C.; Loopstra, B. O. On the uranates of ammonium—II: X-ray investigation of the compounds in the system NH3-UO3-H2O. *J. Inorg. Nucl. Chem.* **1963**, *25*, 945−953.
(37) Cordfunke, E. H. P. On the uranates of ammonium—I: The ternary system NH3—UO3—H2O. *J. Inorg. Nucl. Chem.* **1962**, *24*, 303−307.
(38) Eloirdi, R.; Ho Mer Lin, D.; Mayer, K.; Caciuffo, R.; Fanghänel, T. Investigation of ammonium diuranate calcination with high-temperature X-ray diffraction. *J. Mater. Sci.* **2014**, *49*, 8436−8443.
(39) Andresen, A. F. IUCr, The structure of U3O8 determined by neutron diffraction. *Acta Crystallogr.* **1958**, *11*, 612−614.
(40) Belbeoch, B.; Piekarski, C.; Perio, P. Structure d'U4O9. *Bulletin de Minéralogie.* **1960**, *83*, 206−208.
(41) Wasserstein, B. Cube-Edges of Uraninites as a Criterion of Age. *Nature* **1951**, *168*, 380−380.
(42) Olsen, A. M.; Schwerdt, I. J.; Richards, B.; McDonald, L. W. Quantification of high temperature oxidation of U3O8 and UO2. *J. Nucl. Mater.* **2018**, *508*, 574−582.
(43) Abbott, E. C.; Brenkmann, A.; Galbraith, C.; Ong, J.; Schwerdt, I. J.; Albrecht, B. D.; Tasdizen, T.; McDonald, L. W. Dependence of UO2 surface morphology on processing history within a single synthetic route. *Radiochim. Acta* **2019**, 1121.
(44) Mikhajlov, Y. N.; Gorbunova, Y. E.; Stolyarov, I. P.; Moiseev, I. I. The synthesis and structure of new modification of monoaquadi-fluorouranyl hydrate. *Zhurnal Neorganicheskoj Khimii.* **2002**, *47*, 1980−1986.
(45) Wyckoff, R.W.G. *Crystal structures*; 2nd ed., Interscience Publishers: New York, NY, 1963.
(46) Tamasi, A. L.; Cash, L. J.; Eley, C.; Porter, R. B.; Pugmire, D. L.; Ross, A. R.; Ruggiero, C. E.; Tandon, L.; Wagner, G. L.; Walensky, J. R.; Wall, A. D.; Wilkerson, M. P. A lexicon for consistent description of material images for nuclear forensics. *J. Radioanal. Nucl. Chem.* **2016**, *307*, 1611−1619.
(47) Yato, T.; Tanaka, H.; Kikuchi, T.; Onoshita, T. *Method of preparing uranium dioxide powder from uranium hexafluoride*; 1987. https://patents.google.com/patent/US4963294/en (accessed October 10, 2022).
(48) Kolmogoroff, A. Confidence Limits for an Unknown Distribution Function. *Ann. Math. Stat.* **1941**, *12*, 461−463.
(49) Reneau, S.; Hagan, R.; Harrington, C.; Raymond, R. Scanning Electron Microscopic Analysis of Rock Varnish Chemistry for Cation-Ratio Dating: An Examination of Electron Beam Penetration Depths. *Scanning Microsc.* **1991**, 5.
(50) Ogata, S.; Homma, S.; Sasahira, A.; Kawamura, F.; Koga, J.; Matsumoto, S. Fluorination reaction of uranium dioxide by fluorine. *J. Nucl. Sci. Technol.* **2004**, *41*, 135−141.
(51) Varga, Z.; Wallenius, M.; Krachler, M.; Rauff-Nisthar, N.; Fongaro, L.; Knott, A.; Nicholl, A.; Mayer, K. Trends and perspectives in Nuclear Forensic Science. *TrAC, Trends Anal. Chem.* **2022**, *146*, No. 116503.
(52) Pointurier, F.; Lelong, C.; Marie, O. Study of the chemical changes of μm-sized particles of uranium tetrafluoride (UF4) in environmental conditions by means of micro-Raman spectrometry. *Vib. Spectrosc.* **2020**, *110*, No. 103145.

https://doi.org/10.1021/acsomega.3c00699
ACS Omega 2023, 8, 16896−16906